ROYAL SOCIETY OF CHEMISTRY

## PAPER

Check for updates

# Sn(OH)$_x$-assisted synthesis of mesoporous Mn-porphyrinic frameworks and their carbon derivatives for electrocatalysis†

Xiaoying Zhang, Luyao Liu, Yu Qiao, Jiaxin Liu, Aiguo Kong (ID) * and Yongkui Shan*

5,10,15,20-Tetrakis (4-aminophenyl) Mn-porphyrin and 2,4,6-trihydroxy-1,3,5-benzenetricarbaldehyde were combined into a new mesoporous organic framework by a Schiff-base-type reaction. Sn(OH)$_x$ helped in improving the yield of this Mn-COF. Further, S-containing dimethyl sulfoxide solvent molecules were tripped in the pores of Mn-COFs. Such heteroatoms-enriched Mn-COFs could be used to fabricate Mn–S–N-doped carbons (Mn–S–N–Cs) with abundant mesopores. In particular, Mn–N$_x$ sites could be partly maintained and highly dispersed on the surface of Mn–S–N–Cs; impressively, Mn–N–S–C-800 could be catalyzed for oxygen electroreduction in both alkaline and acidic media. Its half-wave potential reached 0.86 V in 0.1 M KOH, with a very low yield of HO$_2^-$ (4.02%) and better durability. The thermal conversion of the synthesized mesoporous porphyrinic Mn-COFs provided an efficient strategy for fabricating high-dispersion Mn–N$_x$ sites on mesoporous S and N codoped carbons.

## 1. Introduction

Designable covalent organic frameworks (COFs) have emerged as unique porous materials with low densities, high porosities, and adjustable organic structures.[1–3] Various COFs have been successfully synthesized by performing boronate-, imine-, azine-, phenazine-, imide-, and triazine-type reactions with rigid molecular building blocks.[4–9] Among them, macromolecular porphyrin-based COFs (CPFs) have attracted immense interest because of the effective response to light and electric fields, as well as the efficient biomimetic catalytic performances of porphyrins.[10] Due to the stronger π–π interactions of planar macromolecules, porphyrin units tended to link into two-dimensional (2D) atomic layers and stack into crystalline microporous materials.[11] When these frameworks were applied in catalysis, separation, and gas storage, some shortages such as easily buried active sites and lower mass transportation often needed resolution.[12] In such cases, to induce large-pore mesoporosity in CPFs may be a feasible route for facilitating the exposure of active sites and enhancing their mass transportation.

Recently, the electrocatalysis utilizations of CPFs and their carbon derivatives have received increased attention. CPFs with embedded M–N$_4$ sites have been very attractive for electrocatalysis, typically for oxygen reduction reactions (ORRs).[13] Their carbon derivatives could further improve the ORR electrocatalytic activity and durability. The precasting distribution of heteroatoms in CPFs enabled the resultant carbons to possess numerous heteroatom-doped defects, particularly M–N$_4$ sites.[14] Moreover, the catalyzed-carbonization for porphyrinic frameworks with rigid porous structures is favorable for the graphitization of organic frameworks but with abundant porosity.[15] As a result, several 2D Fe- or Co-CPFs have been reported that can be used to fabricate high-performance carbons for ORR.[16] Although stacked 2D structures resulted in the easy degradation of Fe–N$_4$ and Co–N$_4$ sites and the growth of Fe, Co, and Fe$_3$C nanoparticles, the derived carbons still exhibited impressive activities for ORR.[17,18] In contrast to Fe- and Co-based carbons with high intrinsic activities for ORR, Mn-based carbons are relatively less active for ORR.[19] However, unlike the extensive generation of peroxides over Fe- and Co-based carbons (often 10–30%), Mn-based carbons often produced less peroxides (usually <10%), because Mn ions (dissolved from the catalysts) promoted the fast decomposition of peroxides into highly reactive free radicals.[19] The oxidation attack to the active sites on carbons from peroxides dominantly contributed to the degradation of ORR catalytic activities.[20] Mn-Based carbons might prove to be durable and robust electrocatalysts for ORR if their ORR activities could be remarkably enhanced.[21,22] Very recently, by controlling the atomic dispersion of metallic Mn or embedding Mn-N$_x$ or Mn–N$_x$–O$_x$ sites on carbons, some Mn-based carbons have shown competitive ORR performance to Fe- or Co-based electrocatalysts.[23,24]

If a mesoporous CPF with high-dispersion Mn–N$_x$ moieties could be constructed, its carbon derivatives would yield advanced Mn-based electrocatalytic materials for ORR. Herein,

*School of Chemistry and Molecular Engineering, East China Normal University, 500 Dongchuan Road, Shanghai 200241, P.R. China. E-mail: agkong@chem.ecnu.edu.cn*
†Electronic supplementary information (ESI) available. See DOI: 10.1039/c9dt03085a

by a Schiff-base-type reaction of 5,10,15,20-tetrakis (4-amino-phenyl) Mn-porphyrin (Mn-TAPP) with 2,4,6-trihydroxy-1,3,5-benzenetricarbaldehyde, we constructed a new Mn-porphyrinic framework with precast Mn–N$_4$ sites. Annealing this mesoporous Mn-COFs with tripped dimethyl sulfoxide (DMSO) solvent resulted in the formation of mesoporous Mn–S–N-doped carbons (Mn–S–N–Cs). Sn(OH)$_x$ served as the catalyst in the synthesis of Mn-COFs and templates in the formation of mesoporous Mn–S–N–Cs. The thermal conversion of this special Mn-COF controlled the generation of highly dispersed Mn–N$_x$ sites on Mn–S–N–Cs. This endowed Mn–N–S–C-800 with advanced electrocatalytic properties toward ORR in both alkaline and acidic media, with impressive durability and lower yield of HO$_2^-$.

## 2. Experimental

### 2.1 Synthesis

**2.1.1 Synthesis of Mn-TAPP.** Here, 1.00 g of 5,10,15,20-tetrakis (4-nitrophenyl) porphyrin (TNPP) in 250 mL *N,N*-dimethylformamide (DMF) was stirred for 30 min at room temperature. An ethanol solution (15 mL) containing 5.13 g anhydrous manganese acetate was dripped into the above solution. After stirring for 24 h at room temperature, purple mixtures (Mn-TNPP) were collected by filtering and then drying in a vacuum.

For the preparation of Mn-TAPP, Mn-TNPP was subsequently reduced by Sn chloride dehydrate (SnCl$_2$). Typically, SnCl$_2$ as a reducing agent (4.30 g) dissolved in 10 mL HCl (12 M) was dropped into 100 mL HCl solution (12 M) containing 1.02 g Mn-TNPP. The reaction mixtures were stirred for 2.5 h at room temperature and then further heated at 70 °C for 0.5 h under a N$_2$ atmosphere. The cooled mixtures were poured into a beaker with water (100 mL). The pH of this solution was adjusted to 8–9 with ammonia (25 wt%), thereby yielding Sn(OH)$_x$. The mixtures of Mn-TAPP and Sn(OH)$_x$ were collected as blue-purple solids as the precursors of COFs.

**2.1.2 Synthesis of Mn-COFs and Mn–S–N–Cs.** Here, 0.1 g of Mn-TAPP@Sn(OH)$_x$ and 0.12 g of 2,4,6-trihydroxy-1,3,5-benzenetricarbaldehyde (95%) were added in DMSO (60 mL) with 2 ml of acetic acid under a N$_2$ atmosphere. After stirring for 20 min, the reaction mixture was heated at 55 °C for 24 h. The cooled samples were collected by filtering and washing with methanol. The Mn-COF@Sn(OH)$_x$ was finally formed as a jujube red powder with a high yield of about 90%. Mn-COF@Sn(OH)$_x$ was sealed in a quartz tube and heated at 700–900 °C for 4 h under high-purity N$_2$ atmosphere, and the heating rate is 2 °C min$^{-1}$. The obtained samples were leached by stirring in 0.5 M KOH solution for removing the residual Sn species and then underwent a second heat treatment at the same temperature. The final products were named as Mn–S–N–C-$n$ ($n$ is the carbonization temperature). For comparison, Mn-COFs* using Mn-TAPP without the existence of Sn(OH)$_x$ was also prepared; Mn–S–N–Cs* were fabricated under similar thermolysis conditions. The COFs without Mn ions and the derived S–N–Cs were also prepared.

### 2.2 ORR electrochemical experiment

The ORR performance of Mn–S–N–Cs was measured on a CHI-800C electrochemical working station equipped with a three-electrode system. The Ag/AgCl (3 M) electrode and Pt wire (or graphite rod) were used as the reference and counter electrodes, respectively. A ring-rotating disk electrode (RRDE) (electrode area: 0.2475 cm$^2$; diameter: 5.61 mm) was used as the working electrode. A catalyst ink solution was prepared by dispersing 10 mg of Mn–S–N–Cs in 1.25 mL of ethanol containing 30 µL of 5 wt% Nafion-2-propanol solution. Further, 10 µL catalyst ink solution was loaded on the surface of a polished working electrode, followed by drying under infrared light. The catalyst loading of the working electrode was 0.30 mg cm$^{-2}$ in 0.1 M KOH electrolyte and 0.6 mg cm$^{-2}$ in 0.1 M HClO$_4$ solution. For Pt/C, this value is 0.1 mg cm$^{-2}$ for both the electrolytes.

The ORR performance of Mn–S–N–Cs was studied using cyclic voltammetry (CV) and RRDE techniques at a scan rate of 5 mV s$^{-1}$. All the potentials were converted into reversible hydrogen electrode (RHE) potentials (Fig. S1†). Linear sweep voltammetry (LSV) curves were replotted as over-potential ($\eta$) *versus* log current (log $j$) to get Tafel plots for the quantification of ORR kinetics. By fitting the linear part of the Tafel plots, the Tafel slope ($b$) and exchange current density ($J_0$) were determined from the corresponding Tafel equations ($\eta = a + b \log(j)$; $\log J_0 = -a/b$). The corresponding number of transferred electrons ($n$) and HO$_2^-$% yield during the ORR were calculated by using the following equations:

$$n = 4 \times \frac{I_d}{I_d + I_r/N} \quad HO_2^-\% = 200 \times \frac{I_r/N}{I_d + I_r/N}.$$

Electrochemical impedance spectroscopy (EIS) was conducted in O$_2$-saturated 0.1 M KOH solution. The Nyquist diagrams were obtained in the frequency range of $10^5$–$10^{-2}$ Hz at the sinusoidal potential amplitude of ±10 mV.

### 2.3 Characterization

X-ray diffraction patterns (XRD) were acquired on a Rigaku Ultima VI powder diffractometer with Cu-Kα radiation at a scanning rate of 10° min$^{-1}$. Solid-state $^{13}$C NMR of Mn-COFs was performed on a German Bruker Avance III 400 MHz nuclear magnetic resonance instrument. The X-ray photoelectron spectroscopy (XPS) with an Al-Kα X-ray source was performed to determine the surface composition. Fourier-transform infrared (FT-IR) spectra were recorded on an infrared spectrophotometer (Bruker Tensor 27 with KBr pellets). The specific surface areas and pore size distributions were determined by N$_2$ adsorption–desorption on a Quadrasorb evo analyzer at 77 K. The microstructures were observed with a JEM-2100F transmission electron microscope (TEM) operated at 200 kV. Sub-angstrom resolution HAADF-STEM was performed using a FEI-F30 TEM instrument. Raman spectra were obtained by using a GX-PT-1500 (150) apparatus with a 532 nm excitation laser.

# 3.   Results and discussion

## 3.1   Synthesis of Mn-COFs

In the FT-IR spectrum of TNPP, the characteristic skeletal vibrations of the porphyrin ring and nitroso group occur at 1522 and 1399 cm$^{-1}$ (ref. 25) (Fig. 1A-a). After reacting with MnCl$_2$, Mn($\mathrm{II}$) coordinates to pyrrole-nitrogen atoms in TNPP to form Mn–N$_4$ sites; this is confirmed by the characteristic IR vibration band observed at 736 cm$^{-1}$ (ref. 26) (Fig. 1A-b). The UV–vis diffuse reflectance spectrum of TNPP revealed that the Soret band located at 356 nm and the Q bands centered at 521, 563, 595, and 652 nm are characteristic of porphyrin compounds. In contrast to the UV–vis spectra of TNPP and Mn-TNPP (Fig. 1B), it is evident that the two Q bands of Mn-TNPP from the a$_{2u}$(π)–e$_g$*(π) transition (500–700 nm) disappeared. This phenomenon corresponded to the formation of M–N$_4$ moieties in the center of the porphyrin ring owing to the increased Mn-porphyrin molecular symmetry and degeneracy

of the electronic transition levels.[27] After undergoing further reduction of SnCl$_2$, the N–O vibration signals of the –NO$_2$ groups in Mn-TNPP disappeared, accompanied by –NH$_2$ peaks of Mn-TAPP observed at 3380 cm$^{-1}$ (ref. 28) (Fig. 1A-c).

The synthesized Mn-TAPP could react with 2,4,6-trihydroxy-1,3,5-benzenetricarbaldehyde to yield Mn-COFs by a Schiff-base-type aldimine condensation reaction. The structural integrity of the as-synthesized Mn-COFs was confirmed from their FT-IR and solid-state $^{13}$C NMR spectra.[29] As shown in Fig. 1C, the carbon resonance signal at around 177 ppm for Mn-COFs could be attributed to the formation of the C=N bond from the reaction of –NH$_2$ and –CHO.[30] In the FT-IR spectrum (Fig. 1A-d), an absorption band appeared near 1610 cm$^{-1}$ of the C=N bond stretching modes, together with the disappearance of the N–H stretching modes (3380 cm$^{-1}$) of Mn-TAPP building blocks.[31] Some DMSO solvent molecules were tripping into pores or grafting onto frameworks of Mn-COFs, providing the S source for the formation of S-doped
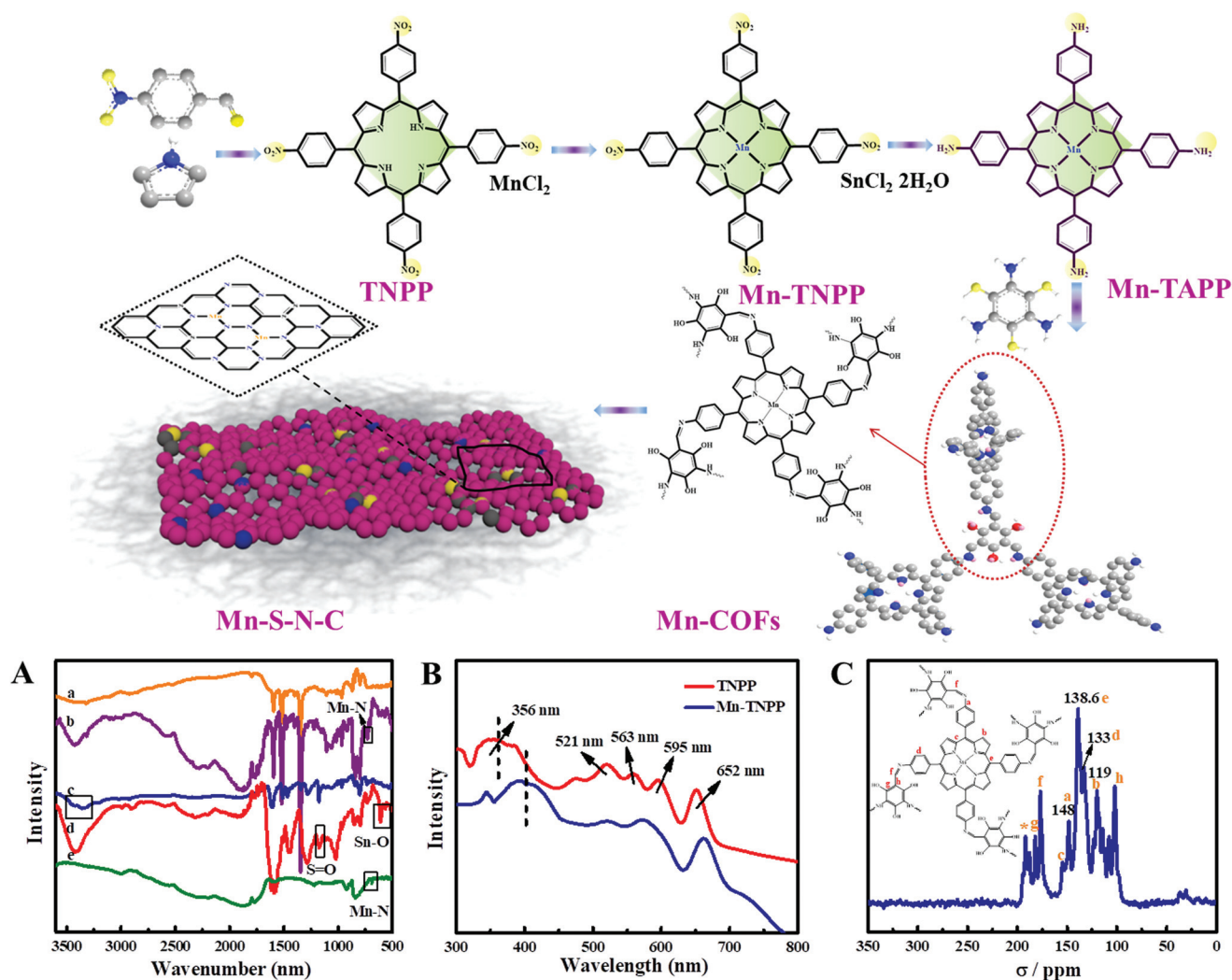


**Fig. 1**  (A) FT-IR spectra of TNPP (a), Mn-TNPP (b), Mn-TAPP (c), Mn-COF (d), and Mn−S−N−C-800 (e). (B) UV−vis diffuse reflectance spectra of TNPP and Mn-TNPP. (C) $^{13}$C solid-state CP-MAS NMR spectrum of Mn-COFs. Note: * corresponds to sidebands that appeared during NMR measurements.

carbon sites. The signal of the S=O stretching vibration at 1176 cm$^{-1}$ also affirmed the existence of S species (Fig. 1A-d).[32]

The SnCl$_2$ agents for reducing –NO$_2$ to –NH$_2$ were finally converted into Sn(OH)$_x$ species by reacting with aqueous ammonia, which remained in Mn-TAPP and formed Mn-COFs. In the synthesis of Mn-COFs, it was found that the residual Sn(OH)$_x$ in Mn-TAPP could efficiently facilitate the production of Mn-COFs. The yield of Mn-COFs reached about 90% within 24 h in the presence of Sn(OH)$_x$. However, the yield of Mn-COFs* was only about 65% after reacting for 24 h under the same conditions if Sn(OH)$_x$ was completely removed. Sn(OH)$_x$ might promote the separation of water from solvents (such as zeolites) and speed up the aminoaldehyde condensation reaction. In fact, Sn(OH)$_x$ residues in Mn-COFs could also be used as hard templates in the carbonization of Mn-COFs, as discussed below.

The TEM images of Mn-COFs revealed that particles on the surface of Mn-COFs were not very large (Fig. S2A and B†). However, a careful observation revealed the presence of a spot of tiny Sn(OH)$_x$ particles. These particles were not observed in the Mn-COFs* images (Fig. S2C†). The N$_2$ sorption analysis for Mn-COFs at 77 K revealed its mesopore-dominated porosity with pore size centered at 2.47 nm. The Brunauer–Emmett–Teller (BET) surface area was calculated to be about 224 m$^2$ g$^{-1}$, while this value for Mn-COFs* was only 142 m$^2$ g$^{-1}$ without Sn(OH)$_x$ (Fig. S3A†). The mesoporosity of Mn-COFs might facilitate the generation of abundant mesopores in the resultant Mn–N–S–Cs and therefore enhance their mass transportation properties.

### 3.2 Synthesis and structure of Mn–S–N–Cs

By directly annealing Mn-COFs, Mn–S–N–C catalysts were successfully prepared. No Mn$_x$O$_y$ or metallic Mn diffraction peaks existed in the XRD patterns of Mn–S–N–Cs; instead, a broad carbon diffraction signal appeared at about $2\theta$ = 24° (Fig. 2A). The XRD patterns revealed the slightly stronger diffraction peaks of Mn–S–N–Cs with an increase in the annealing temperatures. The high dispersion and strong N coordination of Mn(II) in the Mn-COFs deterred the aggregation of Mn species or growth of metallic Mn particles, which resulted in Mn–N$_x$ sites or the possibly metallic Mn nanoparticles in an ultrahigh dispersion state. The Mn–S–N–C-800 sample exhibited sheet-like stacked morphology, as observed by TEM (Fig. 3A and B). There were abundant nanoholes in the carbon layers of Mn–S–N–C-800. No nanoparticles could be observed in the HRTEM image (Fig. 3C), which was in agreement with the XRD results. HAADF-STEM measurements were carried out to determine the distributions of Mn, S, and N on the carbons. It can be seen (Fig. 3E–I) that Mn species were homogeneously dispersed on the S and N codoped carbon supports, which might facilitate improvements in the active-site density of the derived carbons.

Raman spectroscopy was applied to study the degree of defects and graphitization of the as-synthesized samples.[33] As shown in Fig. 2B, the Raman spectra of all the three samples exhibited three clear peaks at around 1344, 1584, and 2800 cm$^{-1}$, attributable to D, G, and 2D bands, respectively.[34]

The 2D bands of Mn–S–N–Cs were weak and broad, illustrating that the carbon framework was composed of thin layers, consistent with the TEM results. It is well known that the D band is associated with structural defects and the G band is related to the vibration of sp$^2$ carbon hybridization.[35] The $I_D/I_G$ value of Mn–S–N–C-800 was 0.97, suggesting the presence of abundant defects in the carbon lattice but with an appropriate graphitization degree. With an increasing pyrolysis temperature, the $I_D/I_G$ values decreased from 0.98 for Mn–S–N–C-700 to 0.95 for Mn–S–N–C-900. Moreover, in contrast to the $I_D/I_G$ value (0.95) of S–N–C-800 (Fig. S3B†), it can be confirmed that the introduction of Mn(II) in COFs broadens the domains of the graphitic structures. This is also verified by the EIS data (Fig. 2C). The prepared Mn–S–N–C-800 exhibited lower charge transfer resistance ($R_{ct}$ = 13.92 Ω) than that of S–N–C-800 ($R_{ct}$ = 25.44 Ω), indicating the enhanced electron-transport property of Mn–S–N–C-800.

N$_2$ sorption tests were performed to determine the specific surface area and pore size distribution of the Mn–S–N–Cs prepared at different temperatures. The type-IV N$_2$ adsorption/desorption isotherms with distinct hysteresis loops between 0.4–0.8 of $P/P_0$ (Fig. 2D) suggested that all the three samples were mesopore-dominated materials. The BET specific surface area of Mn–S–N–C-800 reached 901 m$^2$ g$^{-1}$, which was much larger than those of Mn–S–N–C-700 (425 m$^2$ g$^{-1}$) and Mn–S–N–C-900 (295 m$^2$ g$^{-1}$) (Table 1). As per the calculations based on the Barrett–Joyner–Halenda (BJH) (Fig. 2E) and Horvath–Kawazoe (HK) models (Fig. 2F), the pore diameter distributions of Mn–S–N–C-800 were centered at 0.45 and 3.81 nm, respectively. These features of Mn–S–N–C-800 favor active-site exposure and efficient mass transfer during the ORR process. It should be noted that Sn(OH)$_x$ in the Mn-COFs acted as the hard template during the pyrolysis of Mn-COFs. The formed Sn-based particles during carbonization may deter the serious sintering of COFs and agglomeration of Mn species. The removal of Sn(OH)$_x$ or Sn nanoparticles resulted in the formation of abundant pores. The prepared Mn–S–N–C-800* by converting Mn-COF precursors without Sn(OH)$_x$ yielded lower specific surface of 426 m$^2$ g$^{-1}$, in contrast to that of Mn–S–N–C-800 (901 m$^2$ g$^{-1}$, Fig. S3C†). Sn(OH)$_x$ in Mn-COF precursors clearly plays an important role in enhancing the surface area of Mn–S–N–C-800.

### 3.3 Surface species of Mn-S–N-Cs

The chemical state and electronic structures on the surface of Mn–S–N–C-800 were further detected by XPS. The survey XPS spectrum of Mn–S–N–C-800 exhibited distinctive peaks of Mn, S, N, O, and C, further demonstrating the doping of Mn, S, and N in Mn–S–N–C-800 (Fig. S3D†). Four characteristic peaks of Mn 2p$_{1/2}$ and 2p$_{3/2}$ were observed in the Mn 2p region at binding energies of 648.5–660 and 637–647 eV, respectively, probably originating from the existence of Mn–N$_x$ sites, including few Mn–O and Mn–S species, in the carbon frameworks[36] (Fig. 2H). It is difficult to distinguish the Mn(0) state in the Mn 2p$_{1/2}$ and 2p$_{3/2}$ XPS spectra, verifying the presence of a marginal amount of the metallic Mn(0) state. The unique
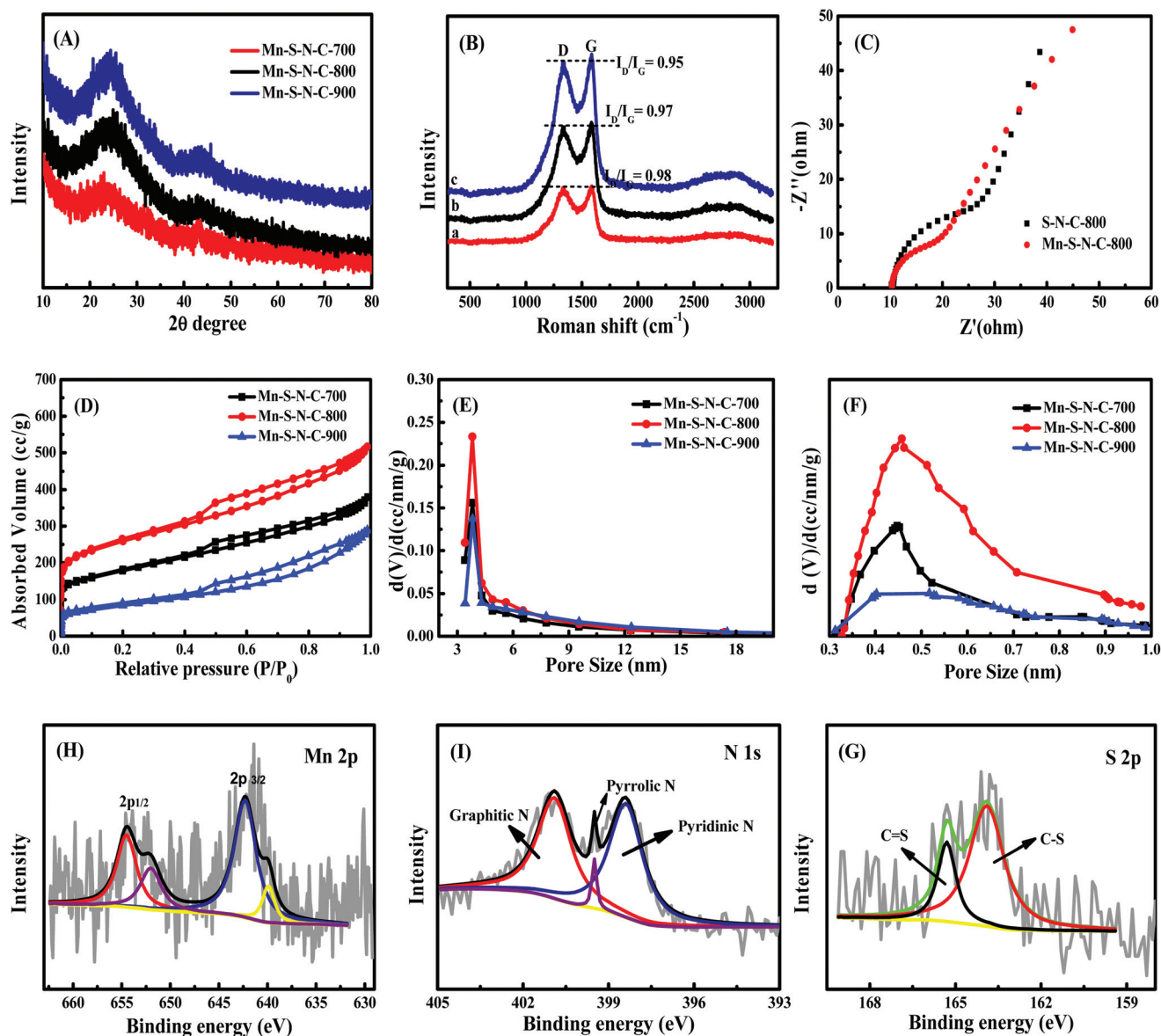
**Fig. 2** (A) Large-angle XRD patterns of Mn−S−N−C-700, Mn−S−N−C-800, and Mn−S−N−C-900. (B) Raman spectra of Mn−S−N−C-700 (a), Mn−S−N−C-800 (b), and Mn−S−N−C-900 (c). (C) Nyquist plots of S−N−C-800 and Mn−S−N−C-800. (D) $N_2$ sorption isotherm curves and the corresponding pore size distribution curves (E and F) of Mn−S−N−C-700, Mn−S−N−C-800, and Mn−S−N−C-900. High-resolution Mn 2p (H), N 1s (I), and S 2p (G) XPS spectra of Mn−S−N−C-800.

Mn−$N_4$ moieties in Mn-COFs can facilitate the maintenance of Mn−$N_x$ sites in Mn−S−N−C-800, instead of decomposition to metallic Mn(0). The high-resolution spectrum for N 1s in Mn−S−N−C-800 could be deconvoluted into pyridinic N (398.4 eV), pyrrolic N (399.5 eV), and graphitic N (400.9 eV)[37] (Fig. 2I). Pyridinic N and graphitic N were demonstrated to change their chemical environment and electron distribution of carbon atoms around them, whereas pyridinic N and pyrrolic N could be coordinated to Mn(II) to form Mn−$N_x$ sites. S atoms have also been doped into carbons along with the decomposition of DMSO solvent residues. The high-resolution S 2p XPS spectrum confirmed that S species mainly entered into the carbon skeleton in the forms of C=S and C–S–C[38] (Fig. 2G).

### 3.4 ORR performance

The ORR electrocatalytic activities of Mn−S−N−Cs were determined by anodic polarization scans in 0.1 M KOH and $HClO_4$. The CVs of Mn−S−N−C-800 exhibited a legible irreversible reduction signal at about 0.88 V under $O_2$-saturated conditions, whereas no distinctive faradaic redox current was detected from the CVs under $N_2$ (Fig. 4A). The LSV curve of Mn−S−N−C-800 depicted the positive half-wave potential ($E_{1/2}$) of 0.86 V, which was 20 mV more positive than that of commercial Pt/C (Fig. 4B). The onset ORR potentials over Mn−S−N−C-800 reached 0.97 V, indicating highly intrinsic activity of Mn−S−N−C-800 for ORR. When the same mass loadings of 0.1
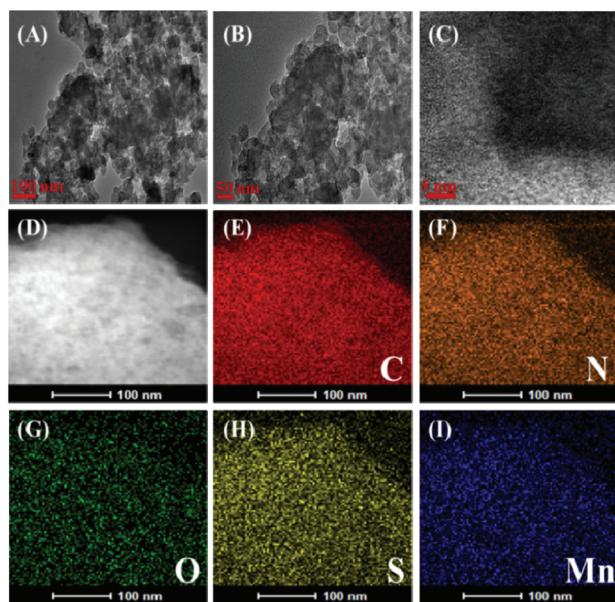
**Fig. 3** (A) and (B) are TEM images of Mn–S–N–C-800. (C) HRTEM images of Mn–S–N–C-800. (D) HADDF image of Mn–S–N–C-800. (E–I) TEM-mapping images of C, N, O, S and Mn.

and 0.3 mg cm$^{-2}$ were used for the Pt/C and Mn–S–N–C-800 electrodes, respectively, the prepared Mn–S–N–C-800 (Fig. S4C and D†) also demonstrated more positive $E_{1/2}$ values than those of Pt/C in 0.1 M KOH, suggesting the more efficient ORR catalytic activity of Mn–S–N–C-800 in alkaline media.

The favorable ORR performance of Mn–S–N–C-800 is enhanced by 10–50 mV, which becomes comparable to the performance of Mn-based ORR catalysts with loading of more than 0.3 mg cm$^{-2}$ (Table S1†).

The efficient ORR activity of Mn–S–N–C-800 is further supported by the smaller Tafel slope of 79 mV dec$^{-1}$, which is in contrast to those of Mn–S–N–C-700 (92 mV dec$^{-1}$) and Mn–S–N–C-900 (88 mV dec$^{-1}$) (Fig. 4C). The Tafel slope of Mn–S–N–C-800 is close to that of Pt/C (74 mV dec$^{-1}$). Moreover, contrast experiments with a graphite rod as the counter electrode were carried out to investigate the electrocatalytic activity of the Mn–S–N–C-800 catalyst for ORR. From Fig. S4A and B,† it is evident that the differences in ORR performance and stability of the Mn–S–N–C-800 catalyst with a graphite rod or a Pt wire as the counter electrodes are negligible in 0.1 M KOH. The prepared Mn–S–N–C-800 clearly behaved as advanced ORR electrocatalysts in alkaline media.

The previously reported Mn$_x$O$_y$ and Mn alloy load-type catalysts often suffer from severe degradation in ORR performance in acidic media due to the inherent reactivity of metallic Mn and their oxides.[23] It is worth noting that Mn–S–N–Cs without the Mn(0) state might improve the stability of Mn-based electrocatalysts in acidic electrolytes as a result of the strong chelating effect on the heteroatoms (e.g., N and S). An obvious cathodic ORR peak at the potential of 0.74 V for Mn–S–N–C-800 loading with 0.6 mg cm$^{-2}$ can be observed in O$_2$-saturated 0.1 M HClO$_4$ solution (Fig. 4D). Mn–S–N–C-800 revealed the $E_{1/2}$ potential of 0.62 V, with a limit current density of 4.7 mA cm$^{-2}$ (Fig. 4E). The ORR peak potential in the CV curves of Mn–S–N–Cs did not generate attenuation before and after 5000 cycles in 0.1 M HClO$_4$. This verified the efficient ORR activity of Mn–S–N–C-800 with better durability in acids (Fig. 4F).

Mn–S–N–C-800 exhibited 10–50 mV more positive $E_{1/2}$ values than those of Mn–S–N–C-700 and Mn–S–N–C-900 in both the electrolytes. Mn–S–N–C-$n$ possessed similar morphology as that observed by TEM (Fig. S6†). However, Mn–S–N–C-800 prepared at an optimum temperature exhibited a larger surface area (901 m$^2$ g$^{-1}$) and more abundant mesoporosity, together with an appropriate graphitization degree. For the surface active species (Fig. S7†), with an increase in the heat-treatment temperature, the surface N content on Mn–S–N–Cs decreased from 5.96 at% for Mn–S–N–C-700 and 5.20 at% for Mn–S–N–C-800 to 2.24 at% for Mn–S–N–C-900 (Table S2†). There is a large decrease in the surface N content of Mn–S–N–C-900 after it undergoes pyrolyzation at 900 °C. A similar degradation for surface S content was also observed from 0.82 and 0.14 to 0.10 at% for the three corresponding samples. The surface Mn content is about 0.54 at% for Mn–S–N–C-700. With the volatilization of the thermal decomposition products and the carbonization of organic frameworks at elevated temperatures, the surface Mn content increased to 1.19 at% for Mn–S–N–C-800. However, the higher annealing temperature of 900 °C caused the serious degradation of Mn–N$_x$ moieties and formed small-size Mn particles encapsulated in carbons. This complicated the detection of carbon-encapsulated Mn nanoparticles by the XPS technique. A lower surface Mn content (0.2 at%) was observed for Mn–S–N–C-900. Higher surface Mn and N contents in Mn–S–N–C-800 might produce more active surface sites for ORR, including the important Mn–N$_x$ sites. The optimized structural properties together with abundant surface Mn and N species generally contribute toward the highest ORR catalytic performance of Mn–S–N–C-800 among these Mn–S–N–C samples.

**Table 1** Textural parameters of Mn-COFs and Mn–S–N–Cs

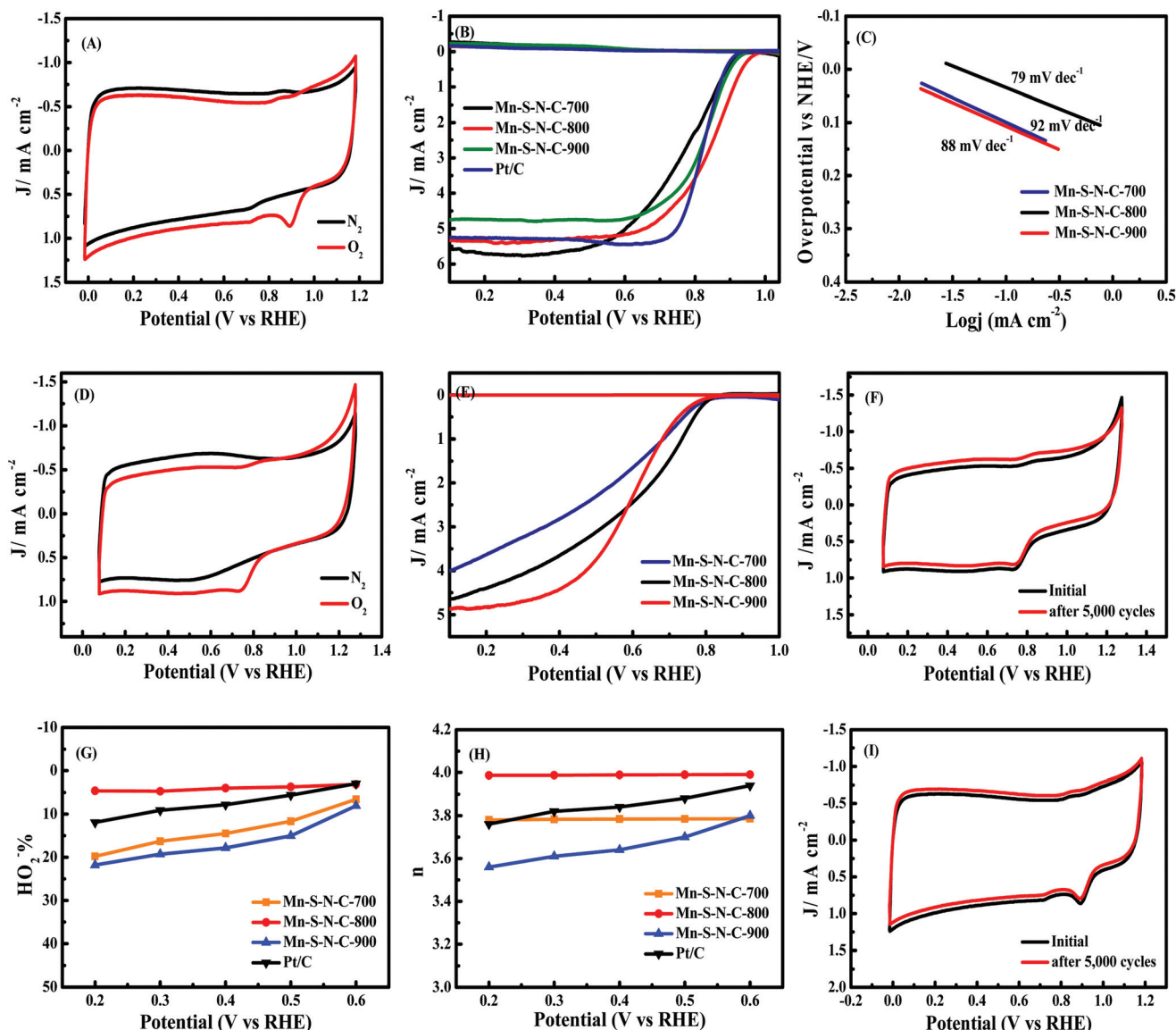| Samples | $S_{BET}$ | $S_{micropore}$ | $S_{exteral}$ | $V_{total}$ | $V_{micropore}$ | $d_{HK}$ | $d_{BJH}$ |
|---|---|---|---|---|---|---|---|
| Mn-COFs | 222 | 20 | 202 | 0.287 | 0.074 | 0.48 | 2.47 |
| Mn–S–N–C-700 | 425 | 7 | 418 | 0.495 | 0.170 | 0.45 | 3.82 |
| Mn–S–N–C-800 | 901 | 304 | 597 | 0.789 | 0.372 | 0.45 | 3.81 |
| Mn–S–N–C-900 | 295 | 83 | 212 | 0.447 | 0.121 | 0.43 | 3.82 |

**Fig. 4** (A) CV curves of Mn–S–N–C-800 in $N_2$- or $O_2$-saturated 0.1 M KOH. (B) RRDE polarization curves and (C) Tafel slopes of Mn–S–N–C-700, Mn–S–N–C-800, and Mn–S–N–C-900. (D) CV curves of Mn–S–N–C-800 in $N_2$- or $O_2$-saturated 0.1 M $HClO_4$. (E) RRDE polarization curves of Mn–S–N–C-700, Mn–S–N–C-800, and Mn–S–N–C-900. (F) CV curves before and after 5000 cycles in 0.1 M $HClO_4$. (G) $HO_2^-$-% yield and (H) number of electron transfers. (I) CV curves before and after 5000 cycles in 0.1 M KOH.

For further investigating the ORR kinetics of Mn–S–N–C-800, RRDE measurements were conducted to determine the reaction mechanism. $H_2O_2$ produced at the disk electrode could be detected by the ring electrode (Fig. 4G). Higher limiting disk current for ORR and very low ring current were observed for the Mn–S–N-800 electrode. Here, n and the percentage of generated $HO_2^-$ are calculated according to the corresponding equations. For Mn–S–N-800, the average value of n is 3.9 in the potential range from 0.2 to 0.6 V (*vs.* RHE), which is close to that for the direct reduction of oxygen (4) (Fig. 4H). The higher yield of $HO_2^-$ would often decrease the electron transfer efficiency and lower the current density, and the $HO_2^-$ species even resulted into the serious degra-

dation of active sites by the oxidation reaction. However, Mn–S–N–C-800 displayed a very low yield of $HO_2^-$ (4.02%). The long-term stability of Mn–S–N–C-800 could be assessed by cycling the catalysts between 0 and 1.2 V (*vs.* RHE). The ORR potential of Mn–S–N–C-800 suffers from a marginal loss after 5000 cycles (Fig. 4I) in 0.1 M KOH and 0.1 M $HClO_4$. This indicated that the lower yield of $HO_2^-$ (4.02%) decreased the decomposition of active sites.

To further explore the main active sites in Mn–S–N–Cs, S–N–C-800 was prepared as a comparative material under the same synthesis conditions. The electrochemical performance of the S–N–C-800 samples is shown in Fig. 5A. There is an oxygen reduction peak at 0.75 V in the CV test, and the ORR
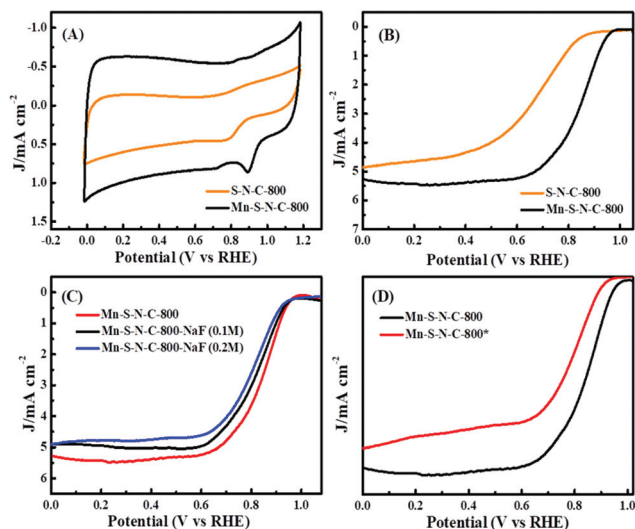
**Fig. 5** CV (A) and LSV (B) curves of S–N–C-800 and Mn–S–N–C-800 in 0.1 M KOH. (C) LSV curves of Mn–S–N–C-800 after poisoning with 0.1 and 0.2 M NaF. (D) LSV curves of Mn–S–N–C-800 and Mn–S–N–C-800*.

half-potential of S–N–C-800 is around 0.7 V; these are about 50 and 160 mV lower than those for Mn–S–N–C-800, respectively (Fig. 5B). This suggested that the Mn atoms in the form of Mn–$N_x$ sites may exert their importance in improving the ORR performance of Mn–S–N–C-800. For further detecting the roles of Mn–$N_x$ sites, $F^-$ ions were added into the electrolytes to poison the Mn–$N_x$ sites by the strong coordination of Mn(II) with $F^-$. After the addition of $F^-$, the ORR half-potential of Mn–S–N–Cs clearly drifted to lower values in both 0.1 M KOH (Fig. 5C) and HClO$_4$ (Fig. S5†), along with remarkable decreases in the corresponding ORR current densities. These results demonstrated that the Mn–$N_x$ sites on the surface of Mn–S–N–C-800 acted as the advantageous active sites for ORR. Moreover, the ORR performance of Mn–S–N–C-800 was comparable to that of Mn–S–N–C-800* prepared without Sn(OH)$_x$. Mn–S–N–C-800* only exhibited half-wave potential of about 0.80 V and current density of about 4.5 mA cm$^{-2}$, which are very different from the corresponding values for Mn–S–N–C-800 (Fig. 5D). This could be attributed to the higher surface area and abundant mesoporosity of Mn–S–N–C-800.

## 4. Conclusions

In summary, a new porphyrinic Mn-COF was synthesized by reacting Mn-TAPP and 2,4,6-trihydroxy-1,3,5-benzenetricarbaldehyde in the presence of Sn(OH)$_x$. By thermally converting such Mn-COFs, mesoporous Mn–S–N–Cs with highly dispersed Mn–$N_x$ sites could be fabricated, which demonstrated efficient activities for ORR in both alkaline and acidic media. The ORR half-wave potential reached 0.86 V in 0.1 M KOH, which makes it one of the best Mn-based ORR electrocatalyst. The Mn–S–N–C-800 catalyst follows a quasi-four-electron transfer pathway

during the ORR process, with very lower HO$_2^-$ yield (4.02%). The thermal conversion of porphyrinic Mn-COFs proved the efficiency of the controlled formation of high-dispersion Mn–$N_x$ sites on S and N codoped carbons with enhanced electrocatalytic properties.

## Conflicts of interest

There are no conflicts to declare.

## Acknowledgements

## Notes and references

1 T. Joshi, C. Chen, H. Li, C. S. Diercks, G. Wang, P. J. Waller, H. Li, J. L. Bredas, O. M. Yaghi and M. F. Crommie, *Adv. Mater.*, 2019, **31**, 1805941.
2 T. Banerjee, F. Haase, S. Trenker, B. P. Biswal, G. Savasci, V. Duppel, I. Moudrakovski, C. Ochsenfeld and B. V. Lotsch, *Nat. Commun.*, 2019, **10**, 2689–2699.
3 M. J. Mancheño, S. Royuela, A. de la Peña, M. Ramos, F. Zamora and J. L. Segura, *J. Chem. Educ.*, 2019, **96**, 1745–1751.
4 Z. Bie, A. Huang, Y. Zhang and Y. Chen, *Anal. Chim. Acta*, 2019, **1065**, 40–48.
5 S. J. Lyle, P. J. Waller and O. M. Yaghi, *Trends Chem.*, 2019, **1**, 172–184.
6 S. Dalapati, S. Jin, J. Gao, Y. Xu, A. Nagai and D. Jiang, *J. Am. Chem. Soc.*, 2013, **135**, 17310–17313.
7 Z. Meng, R. M. Stolz and K. A. Mirica, *J. Am. Chem. Soc.*, 2019, **141**, 11929–11937.
8 H. Fan, J. Gu, H. Meng, A. Knebel and J. Caro, *Angew. Chem., Int. Ed.*, 2018, **57**, 4083–4087.
9 M. Bhadra, S. Kandambeth, M. K. Sahoo, M. Addicoat, E. Balaraman and R. Banerjee, *J. Am. Chem. Soc.*, 2019, **141**, 6152–6156.
10 Z. J. Xia, H. C. Yang, Z. Chen, R. Z. Waldman, Y. Zhao, C. Zhang, S. N. Patel and S. B. Darling, *Adv. Mater. Interfaces*, 2019, **6**, 1900254.
11 T. W. Kim, S. Jun, Y. Ha, R. K. Yadav, A. Kumar, C. Y. Yoo, I. Oh, H. K. Lim, J. W. Shin, R. Ryoo, H. Kim, J. Kim, J. O. Baeg and H. Ihee, *Nat. Commun.*, 2019, **10**, 1873–1883.
12 H. Furukawa and M. Yaghi, *J. Am. Chem. Soc.*, 2009, **131**, 8875–8883.
13 R. Jiang, L. Li, T. Sheng, G. Hu, Y. Chen and L. Wang, *J. Am. Chem. Soc.*, 2018, **140**, 11594–11598.
14 T. Joshi, C. Chen, H. Li, C. S. Diercks, G. Wang, P. J. Waller, H. Li, J. L. Bredas, O. M. Yaghi and M. F. Crommie, *Adv. Mater.*, 2019, **31**, 1805941.
15 S. Rager, A. C. Jakowetz, B. Gole, F. Beuerle, D. D. Medina and T. Bein, *Chem. Mater.*, 2019, **31**, 2707–2712.

16  H. Huang, F. Li, Y. Zhang and Y. Chen, *J. Mater. Chem. A*, 2019, **7**, 5575–5582.

17  F. Kong, X. Fan, A. Kong, Z. Zhou, X. Zhang and Y. Shan, *Adv. Funct. Mater.*, 2018, **28**, 1803973.

18  X. Fan, F. Kong, A. Kong, A. Chen, Z. Zhou and Y. Shan, *ACS Appl. Mater. Interfaces*, 2017, **9**, 32840–32850.

19  L. Wang, A. Ambrosi and M. Pumera, *Angew. Chem., Int. Ed.*, 2013, **52**, 13818–13821.

20  X. Zhu, R. Amal and X. Lu, *Small*, 2019, **15**, 1804524.

21  Z. Huang, X. Qin, X. Gu, G. Li, Y. Mu, N. Wang, K. Ithisuphalap, H. Wang, Z. Guo, Z. Shi, G. Wu and M. Shao, *ACS Appl. Mater. Interfaces*, 2018, **10**, 23900–23909.

22  Y. Zheng, D.-S. Yang, J. M. Kweun, C. Li, K. Tan, F. Kong, C. Liang, Y. J. Chabal, Y. Y. Kim, M. Cho, J.-S. Yu and K. Cho, *Nano Energy*, 2016, **30**, 443–449.

23  Y. Yang, K. Mao, S. Gao, H. Huang, G. Xia, Z. Lin, P. Jiang, C. Wang, H. Wang and Q. Chen, *Adv. Mater.*, 2018, **30**, 1801732.

24  H. Fei, J. Dong, Y. Feng, C. S. Allen, C. Wan, B. Volosskiy, M. Li, Z. Zhao, Y. Wang, H. Sun, P. An, W. Chen, Z. Guo, C. Lee, D. Chen, I. Shakir, M. Liu, T. Hu, Y. Li, A. I. Kirkland, X. Duan and Y. Huang, *Nat. Catal.*, 2018, **1**, 63–72.

25  X. Jiang, Y. Liu, J. Liu, Y. Luo and Y. Lyu, *RSC Adv.*, 2015, **5**, 98508–98513.

26  M. K. Bharty, R. K. Dani, N. K. Singh and R. J. Butcher, *Polyhedron*, 2016, **112**, 67–77.

27  H. M. Wang, J. Q. Jiang, J. H. Xiao, R. L. Gao, F. Y. Lin and X. Y. Liu, *Chem.-Biol. Interact.*, 2008, **172**, 154–158.

28  E.-j. Sun, X.-l. Cheng, D. Wang, X.-x. Tang, S.-j. Yu and T.-s. Shi, *Solid State Sci.*, 2007, **9**, 1061–1068.

29  B. Gole, V. Stepanenko, S. Rager, M. Grune, D. D. Medina, T. Bein, F. Wurthner and F. Beuerle, *Angew. Chem., Int. Ed.*, 2018, **57**, 846–850.

30  S. Haldar, D. Chakraborty, B. Roy, G. Banappanavar, K. Rinku, D. Mullangi, P. Hazra, D. Kabra and R. Vaidhyanathan, *J. Am. Chem. Soc.*, 2018, **140**, 13367–13374.

31  E. Rozhko, A. Bavykina, D. Osadchii, M. Makkee and J. Gascon, *J. Catal.*, 2017, **345**, 270–280.

32  I. P. S. Fernando, K. K. A. Sanjeewa, K. W. Samarakoon, W. W. Lee, H.-S. Kim, E.-A. Kim, U. K. D. S. S. Gunasekara, D. T. U. Abeytunga, C. Nanayakkara, E. D. de Silva, H.-S. Lee and Y.-J. Jeon, *Algae*, 2017, **32**, 75–86.

33  W.-J. Niu, Y.-P. Wang, J.-Z. He, W.-W. Liu, M.-C. Liu, D. Shan, L. Lee and Y.-L. Chueh, *Nano Energy*, 2019, **63**, 103788.

34  Y. Su, S. Li, D. Wu, F. Zhang, H. Liang, P. Gao, C. Cheng and X. Feng, *ACS Nano.*, 2012, **6**, 8349–8356.

35  C. Li, M. Wu and R. Liu, *Appl. Catal., B*, 2019, **244**, 150–158.

36  Z. Yan, H. Qi, X. Bai, K. Huang, Y.-R. Chen and Q. Wang, *Electrochim. Acta*, 2018, **283**, 548–559.

37  Q. Lin, X. Bu, A. Kong, C. Mao, X. Zhao, F. Bu and P. Feng, *J. Am. Chem. Soc.*, 2015, **137**, 2235–2238.

38  W. Yang, L. Chen, X. Liu, X. Yue, C. Liu and J. Jia, *J. Mater. Chem. A*, 2016, **4**, 5834–5838.